Acta Materialia 306 (2026) 121947

Contents lists available at ScienceDirect

Acta Materialia

journal homepage: www.elsevier.com/locate/actamat

Full length article

Solute co-segregation mechanisms at low-angle grain boundaries in magnesium: A combined atomic-scale experimental and modeling study

Risheng Pei [a,*], Joé Petrazoller [b], Achraf Atila [c], Simon Arnoldi [a], Lei Xiao [d], Xiaoqing Liu [e], Hexin Wang [a], Sandra Korte-Kerzel [a], Stéphane Berbenni [b], Thiebaud Richeton [b], Julien Guénolé [b], Zhuocheng Xie [a,*], Talal Al-Samman [a]

[a] Institut für Metallkunde und Materialphysik, RWTH Aachen University, 52056 Aachen, Germany
[b] Université de Lorraine, CNRS, Arts et Métiers Institute of Technology, LEM3, F-57000 Metz, France
[c] Federal Institute of Materials Research and Testing (BAM), Unter den Eichen 87, 12205, Berlin, Germany
[d] School of Materials Science and Engineering, Hefei University of Technology, 230009 Hefei, China
[e] School of Physics and Electronics, Gannan Normal University, 341000 Ganzhou, China

ARTICLE INFO

Keywords:
Atom probe tomography
Atomistic simulation
Grain boundary
Co-segregation
Magnesium alloy

ABSTRACT

Solute segregation at low-angle grain boundaries (LAGBs) critically affects the microstructure and mechanical properties of magnesium (Mg) alloys. In modern alloys containing multiple substitutional elements, understanding solute-solute interactions at microstructural defects becomes essential for alloy design. This study investigates the co-segregation mechanisms of calcium (Ca), zinc (Zn), and aluminum (Al) at a LAGB in a dilute Mg-0.23Al-1.00Zn-0.38Ca (AZX010) alloy by combining atomic-scale experimental and modeling techniques. Three-dimensional atom probe tomography (3D-APT) revealed significant segregation of Ca, Zn, and Al at the LAGB, with Ca forming linear segregation patterns along dislocation arrays characteristic of the LAGB. Clustering analysis showed increased Ca–Ca pairs at the boundary, indicating synergistic solute interactions. Atomistic simulations and elastic dipole calculations demonstrated that larger Ca atoms prefer tensile regions around dislocations, while smaller Zn and Al atoms favor compressive areas. These simulations also found that Ca–Ca co-segregation near dislocation cores is energetically more favorable than other solute pairings, explaining the enhanced Ca clustering observed experimentally. Thermodynamic modeling incorporating calculated segregation energies and solute-solute interactions accurately predicted solute concentrations at the LAGB, aligning with experimental data. The findings emphasize the importance of solute interactions at dislocation cores in Mg alloys, offering insights for improving mechanical performance through targeted alloying and grain boundary engineering.

1. Introduction

Modern metallic alloys are typically composed of multiple alloying elements that enhance desired material properties such as strength, toughness, ductility, and corrosion resistance. While these alloying elements play a crucial role in improving performance, they also introduce complex microstructural interactions across various length scales. Understanding these interactions, particularly at interfaces, is essential for the design and optimization of advanced structural materials with greater strength and ductility [1]. Grain boundaries (GBs), as regions of high lattice disruption, act as thermodynamically favorable sinks for solute atoms due to their higher Gibbs free energy compared to the bulk [2]. Consequently, the concentration of solutes at GBs can significantly exceed their solubility within the grain interior, sometimes by several orders of magnitude [3,4]. Lowering the energy state of the GB network through solute segregation reduces the driving force for capillary-driven grain growth during processing [5].

Beyond thermodynamic stabilization, segregated solute atoms within the GB region exhibit a kinetic effect on the movement of GBs, known as solute drag [6,7]. This effect, influenced by solute diffusivity, retards the mobility of migrating boundaries [8] and can be strategically utilized to control the grain size distribution and texture [9,10]. In this context, recent studies have highlighted that GB solute segregation is influenced by the local GB structure, resulting in a non-uniform distribution of solutes across different boundaries [11]. This variability leads to differing GB mobilities, which in turn facilitates the selective growth of specific texture components [12,13]. In certain cases, solute segregation significantly alters the structural and chemical

* Corresponding authors.
E-mail addresses: risheng.pei@rwth-aachen.de (R. Pei), xie@imm.rwth-aachen.de (Z. Xie).

https://doi.org/10.1016/j.actamat.2026.121947
Received 7 December 2025; Accepted 18 January 2026
Available online 20 January 2026

state of GBs, facilitating the formation of GB secondary phases [14] that further stabilize a fine grain size and enhance material properties through similar kinetic mechanisms like Zener pinning [15].

While most segregation studies have traditionally focused on binary systems, recent research has shifted towards modern multi-component materials [16–20]. The presence of multiple alloying elements can significantly alter the GB segregation behavior, rendering the atomistic mechanisms at interfaces a complex and challenging topic to investigate [21]. Although solute segregation has been well established to enhance GB cohesion and bonding strength [22,23] or induce structural and chemical transitions, resulting in GB-stabilized phases known as complexions [24] or defect phases [25], the study of interactions involving multiple solute species at interfaces remains relatively unexplored. For lightweight materials such as magnesium (Mg) alloys, dilute alloying with specific substitutional solute elements of larger and smaller atomic radii than Mg has been found to extend their utility by improving ductility and yield strength while mitigating mechanical anisotropy [26–28]. In previous research on dilute systems like Mg–Gd–Zn, Mg–Ca–Zn, Mg–Al–Zn–Ca and Mg–Al–Zn–Ca–Y, it was observed that co-added solutes, particularly Zn, can influence and/or compete with the segregation tendencies of the other solute species to GB sites [28–31]. This was evident for elements like Gd and Ca with large atomic sizes. The effect of co-added solutes on segregation, known as synergistic co-segregation, has been recognized in these studies as a beneficial feature for generating unique textures that respond favorably to applied plastic deformation [9,12,26]. Deeper insights into the synergistic nature of co-segregation have revealed that solute clustering and redistribution at GBs depend not only on minimizing elastic strain energy but also on the chemical binding strength with vacancies or co-existing solutes [32,33].

To gain comprehensive insights into the structure and chemistry of GBs with segregated solutes, it is essential to obtain precise and statistically significant experimental data at the atomic scale. Recent advances in characterization techniques, such as aberration-corrected scanning transmission electron microscopy (STEM) [34], transmission Kikuchi diffraction (TKD) [35], and atom probe tomography (APT) [36], have enabled detailed studies of atomic-scale chemical segregation and the crystallography associated with GBs. Utilizing atomic-resolution energy-dispersive X-ray spectroscopy (EDS) at low electron voltages to minimize beam damage, Zhao et al. [17] uncovered a co-segregation pattern characterized by an alternating distribution of large Nd and small Ag atoms fully occupying the $\{10\bar{1}1\}$ and $\{10\bar{1}2\}$ twin boundaries in a Mg–Nd–Ag alloy. First-principles calculations indicated that this segregation pattern strengthens the twin boundary by enhancing bonding, thereby affecting its migration mechanism.

In a study on the effect of co-segregation during annealing of a Mg–Al–Zn–Ca–Y alloy, Pei et al. [29] emphasized that the type and strength of segregation are crucial for restricting the preferential growth of recrystallized grains with a basal texture. Thermodynamically, the synergistic co-segregation of small Al and Zn atoms with large Ca atoms is more effective than mono-segregation in restricting grain growth because co-segregation results in a greater reduction in GB energy, rendering the boundary less mobile.

While high-resolution experimental techniques provide remarkable insights into interface segregation, numerous aspects remain elusive and challenging to capture experimentally. To bridge these gaps, complementary atomic-scale modeling, such as atomistic simulations and density functional theory (DFT) calculations, can be employed to gain a deeper understanding of the underlying processes and mechanisms beyond experimental limitations. A recent review of computational studies on solute segregation presented by Hu et al. [37] highlights significant efforts to investigate substitutional GB segregation. These efforts involve calculating the segregation energy of GB sites across a broad compositional space, revealing a strong correlation between segregation energy and site volume [38–40].

Although numerous studies have explored GB solute segregation in dilute binary solid solutions [41–44], related research has also extended to concentrated solid solutions beyond the dilute limit, accounting for solute-solute [45,46] or even multiple-solute interactions [21,47,48]. Additionally, incorporating vibrational entropy contributions has been shown to enhance predictions of GB segregation energy and solute concentration at elevated temperatures [49,50]. In the context of Mg alloys, most atomic-scale simulations using ab-initio or semi-empirical approaches have traditionally focused on individual GBs, particularly those with highly symmetric tilt configurations [38,39,43,51]. However, to truly understand co-segregation behavior in real, complex materials, it is necessary to consider a much larger number of GB sites and their combinations. This approach demands significantly more computational resources, especially when aiming for DFT-level accuracy [49]. In this regard, Wagih et al. demonstrated that highly symmetric tilt boundaries and low coincidence site lattice (CSL) GBs do not accurately represent polycrystalline GB environments, resulting in incorrect predictions of solute segregation behavior [52]. Building on this understanding, Pei et al. employed APT-informed atomistic simulations to investigate the critical phenomenon of inhomogeneous segregation behavior of Nd at general GBs in as-extruded Mg–Mn–Nd alloys [11]. Their findings revealed that this inhomogeneous segregation within the GB plane arises from local atomic arrangements rather than macroscopic crystallographic characteristics.

The GB segregation energy spectrum and its local atomic environment have been extensively studied in randomly-textured face-centered cubic (FCC) polycrystals. However, polycrystalline Mg, which often exhibits a strong basal texture in conventional sheet alloys, has not received the same level of attention until recently. Recent research by the authors [48] has addressed this gap by calculating the segregation energy spectrum for basal-textured Mg polycrystals, emphasizing contributions from specific GB sites such as triple junctions. The study revealed a distinct bi-modal distribution that significantly differs from the conventional skew-normal distribution observed in randomly oriented polycrystals.

In this study, solute co-segregation mechanisms at a LAGB in magnesium are investigated. The significance of examining solute segregation at LAGBs lies in their prevalence as subgrain structures in deformed materials and their distinct structural characteristics, which differ from those of random high-angle grain boundaries (HAGBs) and highly coherent GBs that have been more extensively studied. LAGBs are characterized by discrete arrays of dislocations resulting from their small misorientation angles (ranging from 5° to 15°), creating unique sites for multiple solute atoms to co-segregate. This segregation notably impacts local strain fields and dislocation mobility, thereby influencing mechanical properties such as yield strength and ductility. By understanding how various solute species interact with different types of GBs, namely LAGBs exhibiting solute-decorated dislocation cores, CSL GBs with precise atomic alignment, or HAGBs with more disordered structures, this research contributes to the development of a comprehensive understanding of how GB structure and characteristics affect solute behavior.

2. Methods

2.1. Experiments

The material investigated in this study was a rare-earth free, lean Mg-0.23Al-1.00Zn-0.38Ca (wt.%) alloy, designated as AZX010, in its as-extruded condition. Following gravity casting and a homogenization treatment at 420 °C for 24 h, the alloy composition was characterized using inductively coupled plasma-optical emission spectrometry (ICP-OES). The alloy was then machined into extrusion billets with an initial diameter of $D_0 = 45$ mm. Hot extrusion was carried out at 250 °C with a speed of 1.0 mm/s, producing extruded bars with a final diameter of

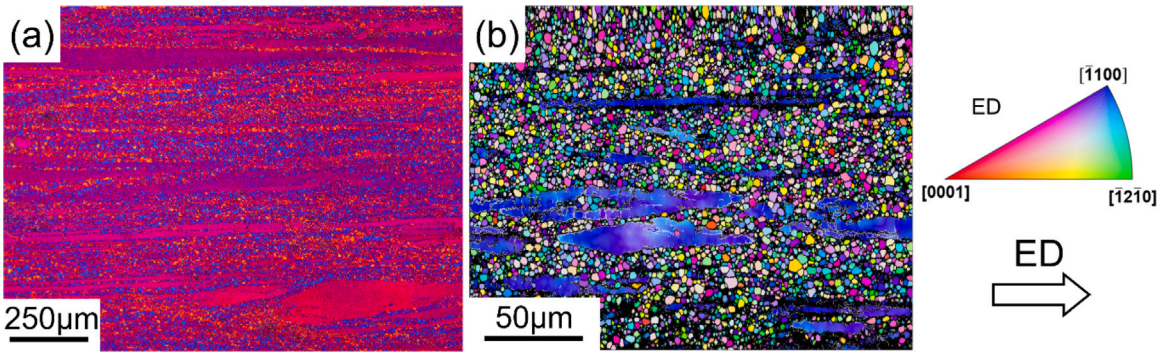

Fig. 1. Microstructure of as-extruded AZX010 alloy: (a) optical microscopic image; (b) EBSD map with IPF coloring with respect to the extrusion direction (ED).

$D_f = 9.0$ mm. This corresponded to an extrusion ratio of $\sim 1:25$ and a logarithmic strain of 3.22, calculated by $\ln\left(\frac{D_0}{D_f}\right)^2$.

The microstructure of the as-extruded sample, characterized using optical microscopy and orientation microscopy via electron backscatter diffraction (EBSD), consists of large elongated grains oriented along the extrusion direction (ED) and small recrystallized grains with an average grain size of 3.2 μm, as depicted in Fig. 1. According to the inverse pole figure (IPF) color coding, the deformed grains are aligned with the $[1\,0\,\bar{1}\,0]$ axis parallel to ED, while the recrystallized grains exhibit random orientations. This indicates a texture modification effect induced by dynamic recrystallization (DRX) and metadynamic recrystallization during hot extrusion and air cooling.

Site-specific preparation of an APT tip lifted out from a deformed region in Fig. 1 was performed by a coordinated process of focused ion beam (FIB) milling and TKD in a FEI Helios 600i dual-beam electron microscope to ensure a precise position of the examined LAGB within the APT tip. Details of this method can be found in [11]. The elemental distributions of solute atoms in the vicinity of the measured LAGB were characterized by 3D-APT in a Local Electrode Atom Probe 4000X HR from Cameca using laser-pulsing mode at a temperature of 30 K. Reconstruction of the evaporated tips was performed using the software package IVAS 3.8.2.

To evaluate the clustering tendency of solute elements in the APT reconstructed sample, we performed a cluster analysis implemented in OVITO [53] using a cutoff distance of 5 Å. The solute clusters containing more than one atom and their compositions were characterized for the GB region and in the matrix.

2.2. Density functional theory calculations

The binding energies of solute pairs in the Mg matrix were calculated using DFT. The calculations followed the methodology outlined in [32] using the Quantum ESPRESSO package [54], employing the projector augmented wave (PAW) method [55,56] and the Perdew–Burke–Ernzerhof (PBE) generalized gradient approximation (GGA) [57] for the exchange–correlation functional. A kinetic energy cutoff of 40 Ry was set for wave functions, while a cutoff of 280 Ry was used for charge densities and potentials. Electronic self-consistency was achieved with a convergence threshold of 10^{-8} Ry. Structural relaxations were conducted using the Broyden–Fletcher–Goldfarb–Shanno (BFGS) relaxation scheme [58], with energy and force convergence thresholds set at 10^{-4} a.u. and 2×10^{-4} a.u., respectively. The orthorhombic simulation cells comprised $5 \times 3 \times 3$ unit cells with 180 atoms using a $4 \times 4 \times 4$ k-point mesh. Solute-solute binding energies were calculated using the following equations:

$$\Delta E_{\text{bind}}^{\text{b,I-J}} = (E_{\text{b}}^{\text{I-J}} + E_{\text{b}}) - (E_{\text{b}}^{\text{I}} + E_{\text{b}}^{\text{J}}), \tag{1}$$

where E_{b} is the energy of the Mg matrix, E_{b}^{I} and E_{b}^{J} are the energies of the Mg matrix containing I and J solutes, respectively, and E_{b}^{I-J} is the energy of the Mg matrix with a solute pair of I and J atoms. Here, a negative binding energy $\Delta E_{\text{bind}}^{\text{b,I-J}}$ indicates an attractive solute interaction, i.e. favorable binding.

2.3. Atomistic simulations

Atomistic simulations were performed using the open-source MD software package LAMMPS [59], employing modified embedded atom method (MEAM) potentials for Mg–Ca–Zn [60], Mg–Ca–Al, and Mg–Zn–Al [61] with identical pair interactions. The potential properties of pure Mg, including elastic constants, stacking fault energies, and GB energies, agree well with the experimental and ab-initio values [38]. Additionally, per-site segregation energies of Ca, Zn and Al solutes at $\Sigma 7$ 21.8° $\{1\,2\,\bar{3}\,0\}$<0001> GB, $\{1\,0\,\bar{1}\,1\}$ and $\{1\,0\,\bar{1}\,2\}$ twin boundaries aligned well with the ab-initio calculations [38]. The binding energies of solute pairs in the Mg matrix were computed using the same $5 \times 3 \times 3$ unit cells as in DFT calculations.

The atomistic configuration of the symmetric tilt LAGB was constructed using Atomsk [63], informed by experimentally determined crystallographic orientations of the grains and GB plane normal to the y-axis. The simulation setup is illustrated in Fig. 2. The orientation was obtained through TKD grain mapping and reconstructed APT tip (shown in Fig. 3). Microscopic degrees of freedom of the LAGB were explored by performing rigid body shift and structural relaxation normal to the GB plane with a force tolerance of 10^{-8} eV/Å using the FIRE algorithm [64,65]. A 2D cylindrical region with a diameter of 18.4 nm and a dimension of 2.4 nm in the periodic direction was cut out in the fully relaxed sample to investigate the segregation behavior at the dislocation array, as shown in Fig. 2b-c. The outermost layers of the cylindrical surface, with a thickness of 1.2 nm (equivalent to twice the interatomic potential cutoff), were constrained in the x and y directions. Periodic boundary conditions were applied along the dislocation line in the z-direction. The boundary effect on calculated per-site segregation energy was found to be negligible, being less than 0.1 meV. Atomistic configurations were visualized using OVITO.

The per-site segregation energy $\Delta E_{\text{seg},i}$ at 0 K for substituting a matrix atom with a solute atom at site i was calculated as:

$$\Delta E_{\text{seg},i} = (E_{\text{GB}}^{i} - E_{\text{GB}}) - (E_{\text{b}}^{i} - E_{\text{b}}), \tag{2}$$

where E_{b}^{i} is the energy of the Mg matrix with one host atom replaced by a solute atom, E_{GB} is the energy of a system with a GB, and E_{GB}^{i} is the energy of the system with a solute atom occupying a GB site or a site in the dislocation core region. In the above-mentioned definition, a more negative value means a higher tendency for segregation.

The solute concentration at GBs is estimated based on its direct link to the per-site segregation energy, as expressed in the spectral segregation model of the Langmuir–McLean isotherm and its White-Coghlan site-based extension [66,67]. For an infinitesimally dilute solid solution, this is represented by:

$$X_{\text{GB},i} = \left(1 + \frac{1 - X_{\text{b}}}{X_{\text{b}}} \exp\left(\frac{\Delta E_{\text{seg},i}}{k_{\text{B}}T}\right)\right)^{-1}, \tag{3}$$

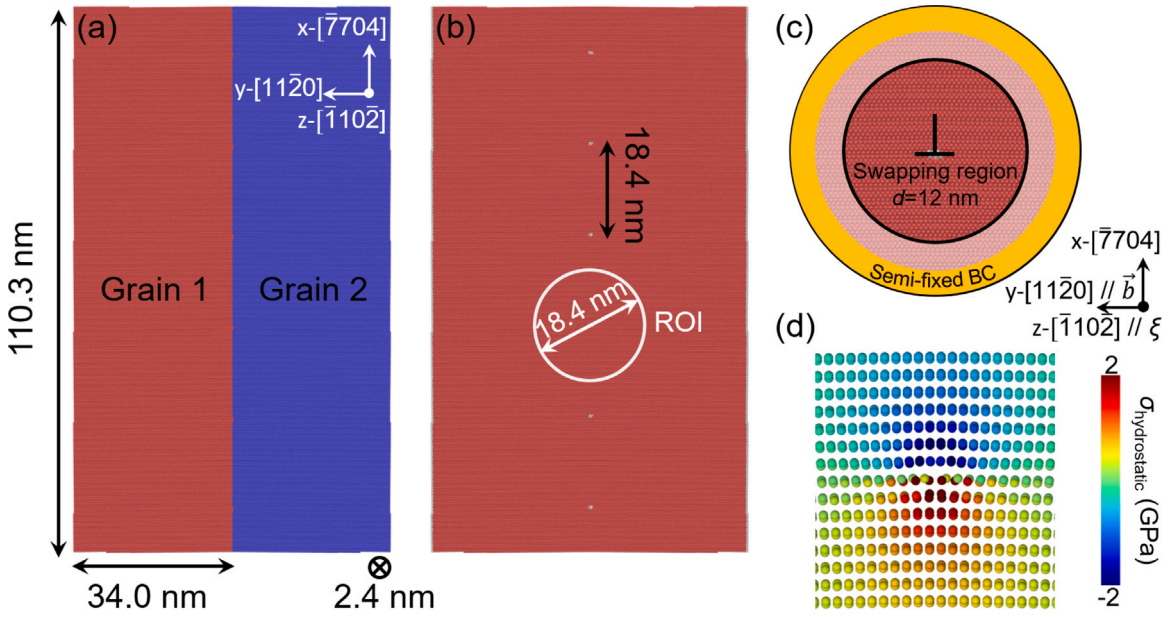

Fig. 2. Atomistic configuration of the symmetric tilt LAGB with a misorientation of 1° along the $[\bar{1}\,1\,0\,\bar{2}]$ rotation axis on the $(1\,1\,\bar{2}\,0)$ GB plane. (a) Slab setup ($110.3 \times 68.0 \times 2.4$ nm^3) of the symmetric tilt LAGB with periodic boundary conditions in x and z directions. (b) The relaxed symmetric tilt LAGB, consisting of an array of edge dislocations with identical core structures and a spacing of 18.4 nm. Atoms are colored according to the common neighbor analysis [62], with white indicating atoms at dislocation cores and red for those in the matrix. (c) Schematic of the cylindrical setup (d=18.4 nm, l_z=2.4 nm) used for solute segregation calculation at the dislocation, featuring semi-fixed boundary conditions (constrained in x and y directions) at outermost layers with a thickness of 1.2 nm. (d) Hydrostatic stress map illustrating the stress fields around the dislocation core region, where blue and red regions represent compressive and tensile stress fields of the edge dislocation, respectively. (For interpretation of the references to color in this figure legend, the reader is referred to the web version of this article.)

where X_b is the bulk solute concentration, and $X_{GB,i}$ is the solute concentration at a specific GB site i. This formulation facilitates the calculation of the weighted average solute concentration at GBs (X_{GB}), given by:

$$X_{GB} = \sum_i F_i X_{GB,i}, \tag{4}$$

where F_i is the fraction of GB sites associated with $X_{GB,i}$. The advantage of this approach is that it directly correlates theoretical predictions from atomic-scale modeling with experimentally measured solute concentrations at GBs through 3D-APT.

3. Results

3.1. 3D-APT characterization of solute segregation to LAGB

For a high-resolution crystallographic analysis of the investigated LAGB, Fig. 3a presents a TKD map of the APT specimen prior to the last annular milling step. To illustrate the lattice distortion within the deformed grain, the IPF color key in the map was limited to a 5° deviation from the average orientation across the entire map. The position of the final needle-shaped volume containing the LAGB is depicted in Fig. 3a, located within 200 nm from the apex. The grain orientations derived from TKD revealed a GB misorientation of 1.08° along $[\bar{1}\,1\,0\,\bar{2}]$, with the GB plane being $(1\,1\,\bar{2}\,0)$. Fig. 3b presents elemental distribution maps for Mg, Ca, Zn and Al atoms within the reconstructed APT tip, indicating solute enrichment of Ca, Zn and Al atoms at the observed LAGB. The morphology of segregated solute regions associated with the LAGB is distinctly visible from a top view of the tip, as illustrated in Fig. 3d. This view reveals parallel linear solute decorations (1.0 at.% Ca iso-surfaces) in the X-Y plane running perpendicular to the major axis of an analyzed cylindrical volume.

The crystallographic analysis shown in Fig. 3c reveals that regions where Ca has segregated lie on the pyramidal $(1\,\bar{1}\,0\,1)$ plane. Fig. 3e provides concentration profiles (at %) of Ca, Zn and Al across these parallel segregated regions within a 30 nm-diameter cylindrical volume outlined in Fig. 3d. The segregation pattern observed in Fig. 3d is interpreted as representing an array of Read–Shockley dislocations lying on the LAGB plane [68]. The quantitative concentration profiles, particularly of Ca, suggest that the segregated region is about 3 nm wide and indicate a spacing of 18.7 ± 0.2 nm between dislocations, as shown in Fig. 3e. The derived misorientation angle from TKD aligns well with the theoretical value determined from the Frank-Bilby formulation [69,70], based on the Burgers vector (b = 0.32 nm) and the distance between edge dislocations in a pure tilt GB:

$$\theta = 2\arcsin\left(\frac{b}{2d}\right) = 0.98 \pm 0.2^\circ \tag{5}$$

Additionally, it is evident that there are variations in segregation levels at each dislocation position within the array plane. These variations might be attributed to defects of atomic dimensions, such as kinks or jogs along the dislocation line.

The average peak concentrations of Ca, Zn, and Al within the dislocation array are listed in Table 1. The measured Ca, Zn, and Al average peak concentrations at the LAGB were 1.29, 1.10, and 0.70 at.%, respectively. Notably, Ca atoms demonstrated a significantly stronger segregation potential with a segregation ratio of 12.56, whereas Zn and Al exhibited similar potentials with segregation ratios of approximately 4.05 and 4.65, respectively. This result is further illustrated in the isosurface maps shown in Fig. 4a-c, where thresholds were set at isoconcentrations of 1.0 at.% for Ca, 1.2 at.% for Zn and 0.8 at.% for Al.

3.2. Cross-scale modeling: Mono-segregation to dislocation array in LAGB

To gain helpful insights into the atomistic mechanisms of solute clustering and segregation at the LAGB, atomistic simulations for dislocation arrays with experimentally informed characteristics were performed.

Fig. 5a-c shows the distribution of per-site segregation energy ΔE_{seg} of segregated Ca, Zn and Al solutes to a model edge dislocation. As

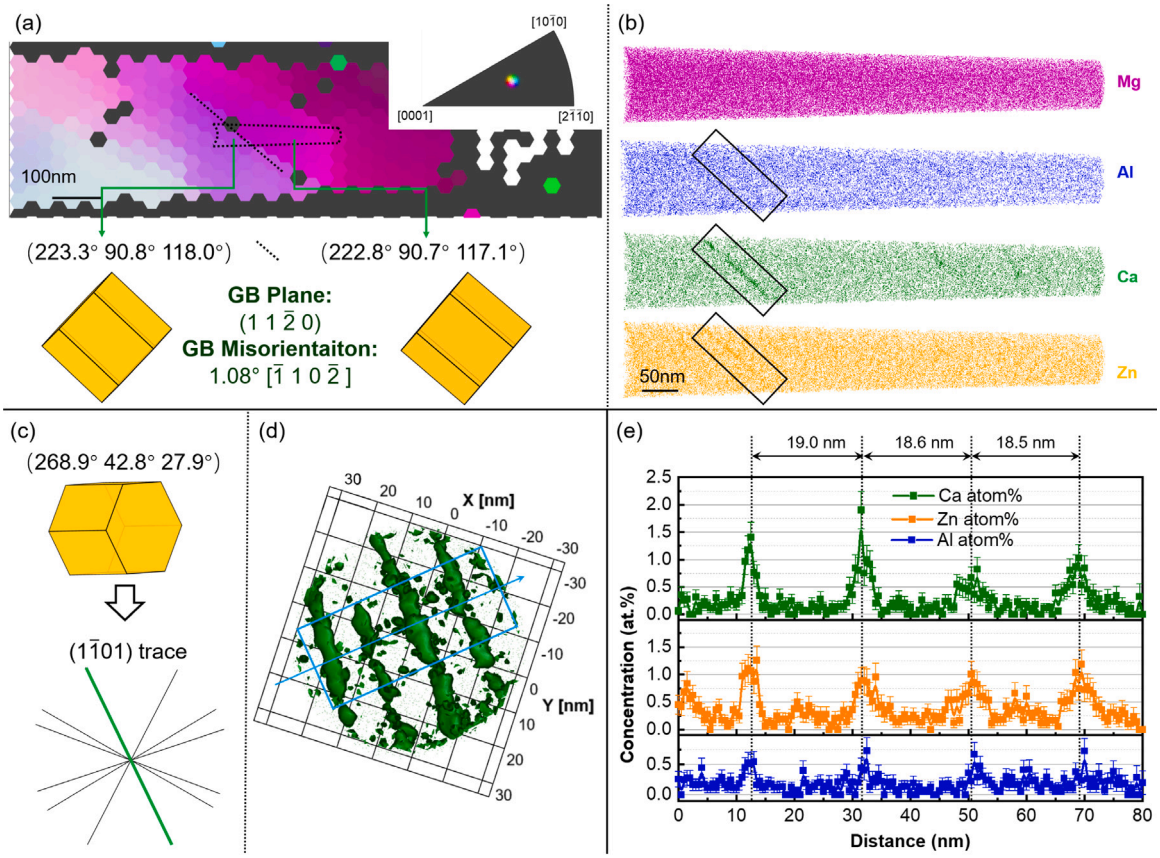

Fig. 3. Chemical analysis of the LAGB in the APT specimen of deformed AZX010 Mg alloy. (a) TKD grain map of the APT specimen, with the IPF color key restricted to a 5° deviation from the average orientation. (b) Elemental distribution maps for Mg, Al, Ca and Zn within the reconstructed volume, highlighting solute segregation at the LAGB in the outlined region. (c) Corresponding grain orientation viewed from the top of the tip and the $\{1\bar{1}01\}$ plane traces calculated based on Euler angles obtained from TKD. (d) 1.0 at.% Ca isosurface (X-Y plane) within the region of interest marked in (b), indicating parallel segregation patterns along line defects in the LAGB. (e) Solute concentration profiles (at.%) across the segregated regions, measured within a cylindrical volume 30 nm in diameter. The profiles reveal periodic segregation with an approximate spacing of 19 nm.

Table 1
Solute concentrations of Ca, Zn and Al within the LAGB obtained from the concentration profiles in Fig. 3d. The positions 1-4 denote the periodic locations along the boundary that are intersected with the array dislocations. Peak concentrations denote the maximum solute concentration measured at the dislocation. Baseline concentrations denote the concentration level away from the peaks, i.e. in the absence of dislocations. SD: Standard deviation.

Position	Ca		Zn		Al	
	Peak	Baseline	Peak	Baseline	Peak	Baseline
# 1	1.43	0.14	1.27	0.22	0.59	0.16
# 2	1.92	0.11	0.95	0.30	0.76	0.15
# 3	0.78	0.06	1.02	0.22	0.68	0.14
# 4	1.02	0.10	1.14	0.34	0.76	0.15
Mean	1.29	0.10	1.10	0.27	0.70	0.15
SD	0.39	0.02	0.11	0.05	0.06	0.005
Segregation ratio (Peak/Baseline)	12.90		4.07		4.67	

depicted in Fig. 2d, Ca solutes exhibit a preference for segregation in the tensile stress field. Conversely, Zn and Al solutes tend to segregate in the compressive stress field. Accordingly, all ΔE_{seg} spectra in Fig. 5d exhibit a bimodal distribution, reflecting the distinct segregation preferences between tensile and compressive stress fields. The ΔE_{seg} distribution for Ca displays a broader peak compared to those of Zn and Al solutes. This difference becomes more apparent when ΔE_{seg} is plotted against the distance from the dislocation core, as shown in Fig. 5e. The ΔE_{seg} values for Ca consistently remain higher in the tensile stress field compared to ΔE_{seg} values for Zn and Al in the compressive stress field. Near the dislocation core, Al shows a slightly stronger segregation tendency than Zn, as evidenced by its more negative ΔE_{seg} values. The simulation results on mono-segregation align well with the experimental observation of solute enrichment at the LAGB, where Ca exhibits a segregation ratio twice that of Zn and Al.

In addition to the segregation energy computed by atomistic simulations, permanent elastic dipole tensors offer valuable insights into the observed mono-segregation behavior within elasticity theory. Elastic dipole calculations, employed as a framework for modeling point defects, correspond to the first moment of the distribution of point forces imposed by a solute atom on its surrounding atoms, reflecting size and shape effects [71–77]. These tensors can be determined through molecular statics simulations based on the residual stress tensor of a bulk lattice containing a single solute [76,78]. The permanent elastic

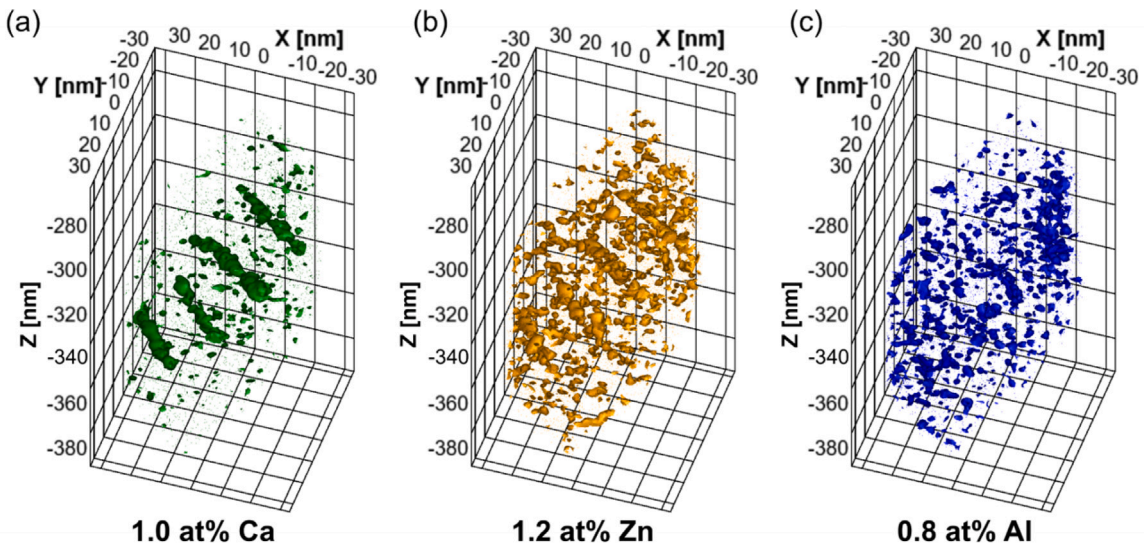

Fig. 4. 3D reconstructions of the isosurfaces in the GB region for Ca (a), Zn (b) and Al (c).

dipole tensors P_{ij}^0 of a single Ca, Zn, and Al solute atom in substitution in the Mg lattice were computed and are presented as follows in the frame $X \parallel [\bar{7}704]$, $Y \parallel [11\bar{2}0]$, $Z \parallel [\bar{1}10\bar{2}]$:

$$\text{Ca in Mg:}\quad P_{ij}^0 = \begin{pmatrix} 3.19 & 0 & 0.03 \\ 0 & 3.18 & 0 \\ 0.03 & 0 & 3.24 \end{pmatrix} \text{(eV)}$$

$$\text{Zn in Mg:}\quad P_{ij}^0 = \begin{pmatrix} -1.70 & 0 & -0.03 \\ 0 & -1.69 & 0 \\ -0.03 & 0 & -1.74 \end{pmatrix} \text{(eV)}$$

$$\text{Al in Mg:}\quad P_{ij}^0 = \begin{pmatrix} -1.63 & 0 & 0.09 \\ 0 & -1.68 & 0 \\ 0.09 & 0 & -1.52 \end{pmatrix} \text{(eV)}$$

The solute segregation preferences observed in atomistic simulations align well with the elastic dipole values. Both Al and Zn exhibit negative principal values that are similar in magnitude, consistent with their comparable segregation field amplitudes in Mg. This consistency extends to Ca, which displays a stronger segregation field intensity with an opposite sign. The elastic dipole values of Ca are indeed positive and higher in magnitude compared to Al and Zn. Additionally, elastic dipole tensors enable the calculation of the interaction energy between a solute atom and the strain field ε_{ij} generated by crystalline defects such as dislocations [72,76,79], using:

$$E^{\text{int}}(x) = -P_{ij}\varepsilon_{ij}(x) \tag{6}$$

The strain field around the dislocation is computed through molecular statics simulations and subsequently interpolated onto a regular grid [78,80]. Fig. 5 then illustrates the interaction energy fields of Ca, Zn and Al solutes as they interact with the dislocation, demonstrating good accuracy of the interaction energy model in capturing the mono-segregation behavior of studied solutes.

3.3. Atomic-scale modeling: Co-segregation to dislocation array in LAGB

In the investigated quaternary alloy system, solute–solute interactions give rise to distinct segregation behaviors for various solute pairs. Fig. 6 schematically summarizes the relevant energy states (E) and corresponding energy differences (ΔE) associated with various segregation scenarios. Four configurations are considered: (i) Two isolated solute atoms (I and J) in the bulk corresponding to an energy state $E_{\text{b}}^{\text{I,J}}$; (ii) a solute pair (I-J) in the bulk ($E_{\text{b}}^{\text{I-J}}$); (iii) two separate solutes (I and J) at the GB ($E_{\text{GB}}^{\text{I,J}}$); and (iv) a solute pair (I-J) at the GB ($E_{\text{GB}}^{\text{I-J}}$) [81,82].

Atomistic simulations were conducted to quantify how these interaction scenarios influence segregation energies for different solute combinations within a 6 nm radius of the dislocation core. One segregation scenario considers a mono-segregation process of individual solute atoms segregating from the bulk to form a solute pair at adjacent sites of the LAGB. The associated energy is defined by Eq. (7):

$$\Delta E_{\text{seg}}^{\text{I-J}\prime} = (E_{\text{GB}}^{\text{I-J}} - E_{\text{GB}}) - (E_{\text{b}}^{\text{I,J}} - E_{\text{b}}), \tag{7}$$

A negative value of $\Delta E_{\text{seg}}^{\text{I-J}\prime}$ indicates that pairing at the LAGB is energetically preferred over pairing in the bulk.

As illustrated in Fig. 7a, Ca–Zn and Ca–Al pairs predominantly exhibit negative $\Delta E_{\text{seg}}^{\text{I-J}\prime}$ values with narrow distributions, signifying favorable segregation and clustering at the dislocation core region of the LAGB. In contrast, Ca–Ca pairs display mainly positive $\Delta E_{\text{seg}}^{\text{I-J}\prime}$ values with a bi-modal distribution. Similarly, Zn–Zn, Al–Zn, and Al–Al pairs also exhibit bi-modal distributions skewed towards the positive side of the distribution indicative of antisegregation. Fig. 7b shows how $\Delta E_{\text{seg}}^{\text{I-J}\prime}$ varies as a function of distance to the dislocation core, providing important insights into spatial segregation tendencies of different solute pairs. For Ca–Ca pairs, segregation is generally unfavorable near the dislocation core. However, in a narrow region extending approximately 8 Åfrom the core, where the tensile stress field is strongest, the segregation energy becomes negative, indicating favorable Ca–Ca segregation. Other Ca-containing pairs such as Ca–Zn and Ca–Al also demonstrate enhanced segregation within this tensile zone. Conversely, Zn–Zn-, Al–Zn-, and Al–Al-containing pairs preferentially segregate into regions characterized by compressive stress near the core.

A second key segregation scenario in accordance with Fig. 6 involves pre-formed solute clusters in the bulk that segregate together to adjacent GB sites in the LAGB. This process is described by Eq. (8) through $\Delta E_{\text{seg}}^{\text{I-J}\prime\prime}$:

$$\Delta E_{\text{seg}}^{\text{I-J}\prime\prime} = (E_{\text{GB}}^{\text{I-J}} - E_{\text{GB}}) - (E_{\text{b}}^{\text{I-J}} - E_{\text{b}}) \tag{8}$$

Negative $\Delta E_{\text{seg}}^{\text{I-J}\prime\prime}$ values indicate that cluster formation at the GB is favored relative to solute clusters in the bulk. Figs. 7c and d reveal that all solute pair distributions of $\Delta E_{\text{seg}}^{\text{I-J}\prime\prime}$ within 6 nm of the dislocation core are centered around zero. However, Ca-Ca pairs display broader distributions than other pairs while both Ca-Zn and Ca-Al pairs exhibit narrow profiles. The remaining combinations maintain bimodal characteristics similar to those observed previously. Consistently across both scenarios, Ca-containing clusters, especially Ca-Ca, preferentially co-segregate into tensile regions of the dislocation field as evidenced by

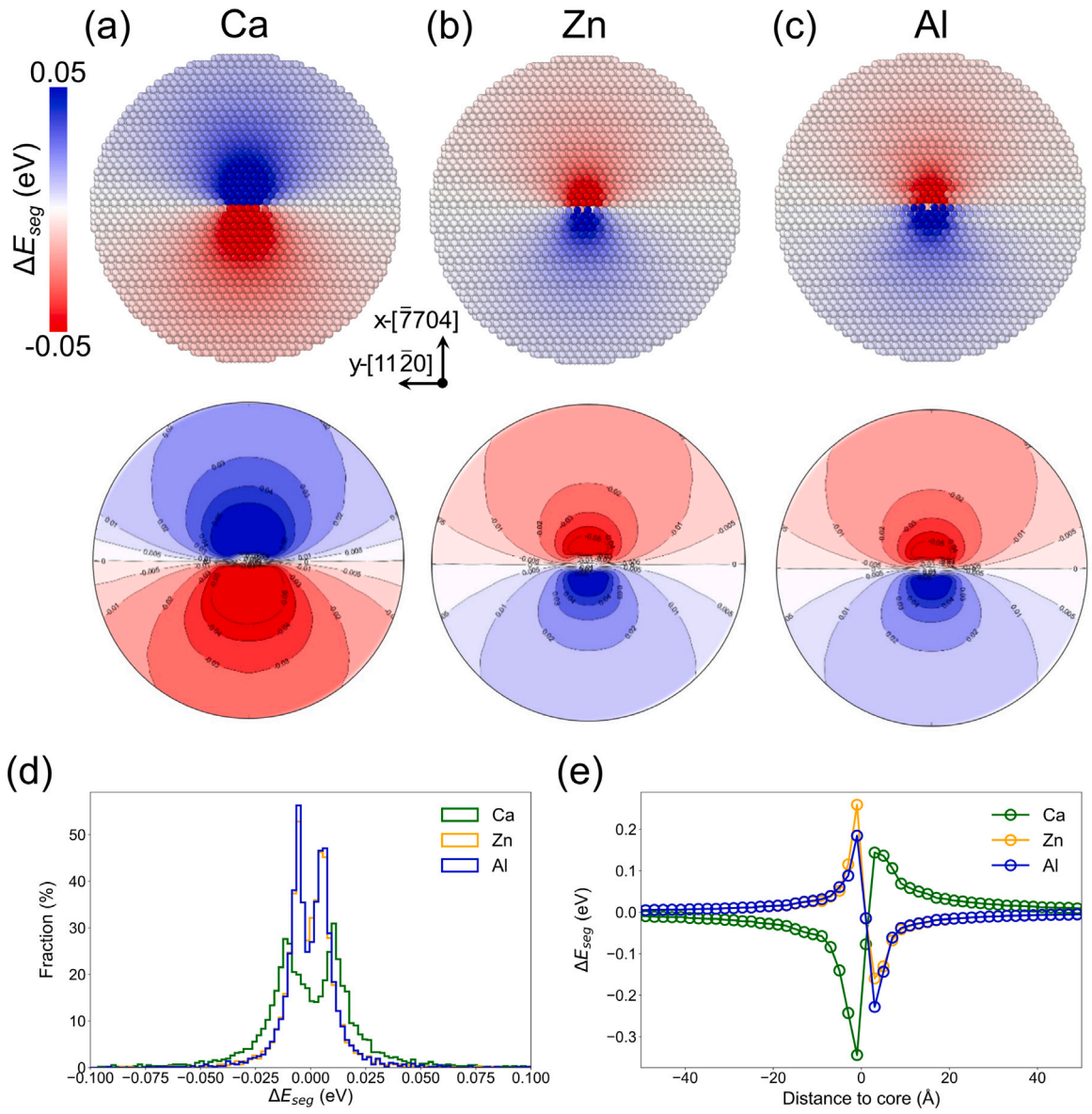

Fig. 5. Mono-segregation behavior of (a) Ca, (b) Zn and (c) Al solutes at the dislocation. Upper row: Atomistic simulations; lower row: Interaction energy fields between the solute modeled as an elastic dipole and the strain field of the dislocation. A negative value of ΔE_{seg} indicates that segregation is energetically favorable. (d) Distribution of ΔE_{seg} for Ca, Zn and Al solutes with data grouped into bins of 2 meV. (e) Statistics of ΔE_{seg} as a function of distance to the center of the dislocation core. Negative distances correspond to the tensile stress region, whereas positive distances indicate the compressive stress region. Data is divided into bins of 2 Å.

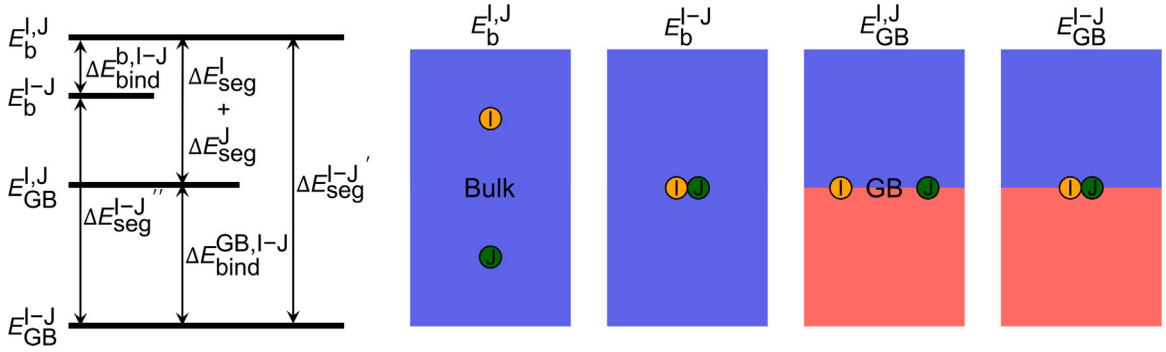

Fig. 6. Schematic illustration of the relationships between energy states (E), segregation energies (ΔE_{seg}), co-segregation energies (ΔE_{seg}^{I-J}), and binding energies (ΔE_{bind}^{I-J}) for solutes I and J in bulk Mg and at the GB.

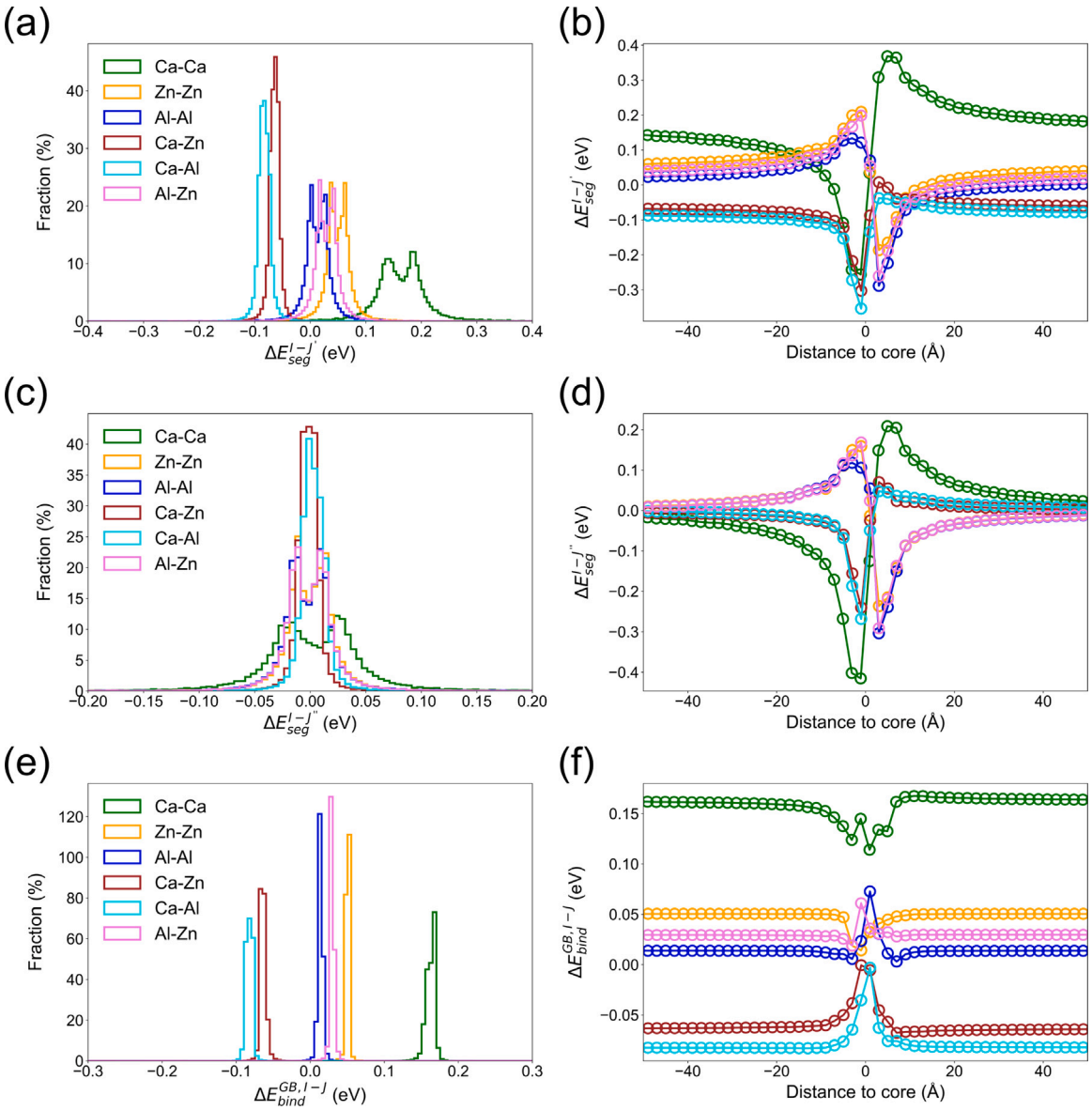

Fig. 7. Atomistic simulations of co-segregation behavior of Ca, Zn and Al solutes at the dislocation. (a) Distribution of $\Delta E_{seg}^{I\text{-}J'}$, and (b) statistics of $\Delta E_{seg}^{I\text{-}J'}$ as a function of distance to the center of the dislocation core. (c) Distribution of $\Delta E_{seg}^{I\text{-}J''}$, and (d) statistics of $\Delta E_{seg}^{I\text{-}J''}$ as a function of distance to the center of the dislocation core. (e) Distribution of $\Delta E_{bind}^{GB,I\text{-}J}$, and (f) statistics of $\Delta E_{bind}^{GB,I\text{-}J}$ as a function of distance to the center of the dislocation core. Negative distances correspond to the tensile stress region, whereas positive distances indicate the compressive stress region. The bin size in (a), (c) and (e) is 5 meV, and in (b), (d), (f) 2 Å.

more negative $\Delta E_{seg}^{I\text{-}J''}$ values. In contrast, Zn-Zn, Al-Zn, and Al-Al pairs favor compressive zones close to dislocation cores.

Finally, we evaluate whether solute pair binding at the GB is energetically preferred over configurations where the solutes are widely separated along distant GB sites. This is quantified by the binding energy $\Delta E_{bind}^{GB,I\text{-}J}$, defined analogously to Eq. (1), where negative values indicate energetic preference for paired configurations along the boundary. Figs. 7e and f present both the binding energy $\Delta E_{bind}^{GB,I\text{-}J}$ distributions and its spatial variation within the dislocation core region. These results reveal which solute pairs are most likely to remain bound at the LAGB, providing insights into their relative stability and interaction tendencies in this environment. For Ca–Ca pairs, binding energies are generally positive near the dislocation but decrease, becoming less positive, as they approach the core. In contrast, Ca–Zn and Ca–Al pairs exhibit negative binding energies that become less negative nearer to the core, indicating a weakening but still favorable tendency for pairing in this region. Zn–Zn pairs behave similarly to Ca–Ca, i.e. their binding energies remain positive but gradually diminish as they approach the dislocation core.

4. Discussion

In this study, APT-informed atomistic simulations were utilized to investigate solute segregation in a dilute AZX010 Mg alloy, specifically focusing on the interactions between solutes and LAGBs at the dislocation core level. APT was crucial for identifying compositionally distinct domains within the investigated sample and clarifying their role in accommodating solute atoms. This joint approach provides a chemically resolved picture of the measured boundary and a mechanistic explanation for the observed segregation behavior.

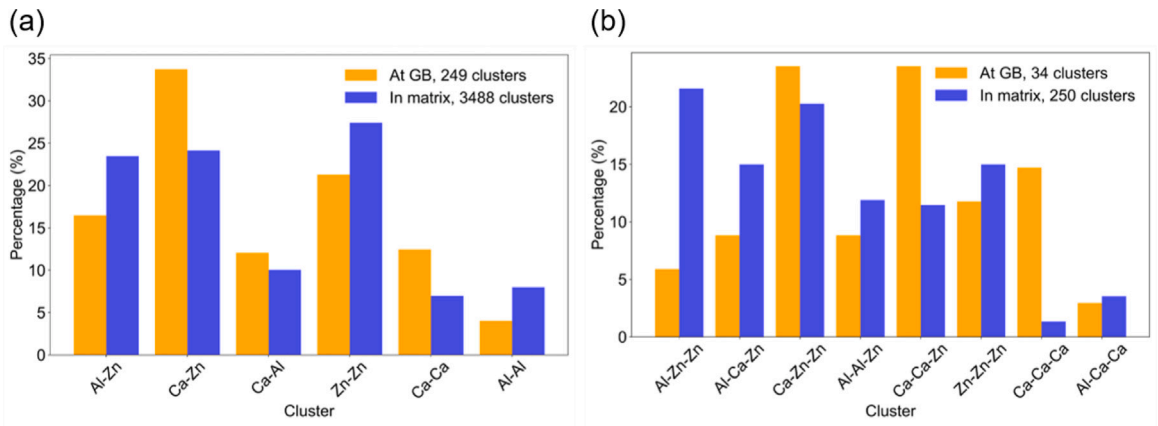

Fig. 8. Clustering analysis of all solute pairs in the APT dataset (d) and the most frequent solute triplets (clusters), both in the matrix and at the GB region, defined by cylindrical areas along the segregated linear regions with a radius of 6 nm.

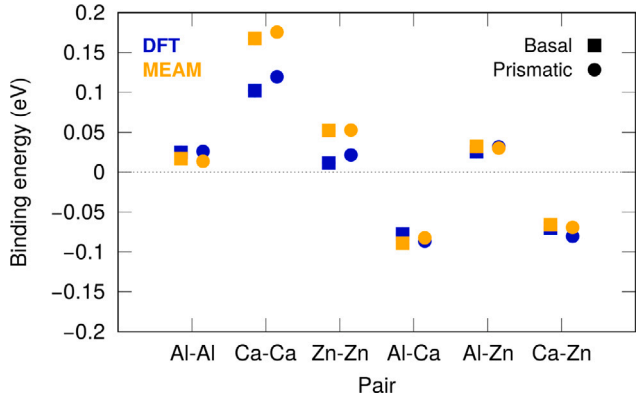

Fig. 9. Binding energies of solute pairs in the Mg matrix (5 × 3 × 3 unit cells) calculated using the MEAM potentials and DFT. The pairs located on a basal (prismatic) plane are represented by a full square (circle).

4.1. Solute distribution and clustering at LAGB

Characterization of the reconstructed atom probe data revealed linear segregation patterns along the boundary, corresponding to periodically arranged dislocation arrays decorated by solutes. The segregation characteristics of solute atoms to the dislocation array are dictated by its binding energy with dislocations, which depends on its atomic size misfit relative to Mg. Al and Zn, both possessing negative misfits, preferentially segregate to regions under compression within the dislocation stress field. In contrast, Ca, with a positive misfit, segregates to regions under tension. This trend is further supported by elastic dipole calculations, from which positive and higher-magnitude dipole values for Ca suggest a stronger interaction with tensile fields. The observed bi-modal distribution of segregation energies (ΔE_{seg}) at the LAGB aligns well with recent findings in basal-textured Mg polycrystals [48], highlighting the role of tilt LAGBs as critical sites for inhomogeneous solute distributions.

Estimating GB solute concentrations using Eq. (3) requires careful selection of appropriate segregation energies among the various scenarios depicted in Fig. 6. At low solute concentrations, where solute–solute interactions are negligible, mono-segregation of individual solutes is typically considered most relevant. However, prior studies on similar systems have shown that solute clustering in both the matrix and at GBs can occur even at relatively low concentrations, leading to co-segregation of clusters rather than isolated atoms [12,32].

To clarify this point, we performed a statistical nearest-neighbor analysis of APT data to quantify differences in solute clustering tendencies between the matrix and GB region. The analysis focused on pairs and small clusters (up to three atoms) within a cutoff distance of 5 Å. The GB region was defined as cylindrical volumes along segregated dislocation lines with a 6 nm radius, while the matrix comprised areas beyond 10 nm from these lines. The results shown in Fig. 8 reveal distinct patterns in clustering behavior. In the matrix, Zn–Zn pairs are most prevalent among all solute pairs, followed by Ca–Zn and Al–Zn pairs, whereas Ca–Ca pairs are least frequent. Near the GB, however, there is a marked increase in Ca–Ca pair fractions from 7% in the matrix to 12.4% at the GB. Other Ca-containing pairs also become more common near the GB. For example, Ca–Zn pairs rise from 24% to 34%. In contrast, Al–Zn, Zn–Zn, and Al–Al pair frequencies decrease within the GB region.

For larger clusters (triplets), Al–Zn–Zn and Ca–Zn–Zn dominate in the matrix alongside Zn–Zn–Zn clusters. At the GB there is a dramatic enrichment of Ca-containing triplets: notably, Ca–Ca–Ca clusters increase from just 1.2% in the matrix to 14.7% at the GB; Ca–Ca–Zn clusters also rise significantly from 10.4% to 23.5%, while Ca–Zn–Zn remain prominent near both regions. Conversely, Al- and Zn-rich triplets such as Al-Zn-Zn decrease sharply near the GB (from 19.6% down to 5.9%).

These observations highlight important synergistic interactions among solutes at LAGBs, most notably the strong attraction of Ca for Zn and Al, which foster increased occurrence of mixed pairs/triplets such as Ca-Zn or Ca–Ca–Zn near the LAGB compared to bulk regions. Such trends point to cooperative co-segregation preferences into specific configurations favored by local chemical environment and binding energetics. Strikingly, both simple and more complex Ca-rich clusters are substantially enriched at the GB compared to their distribution in the bulk, which is also corroborated by experimental APT data.

Whether solute atoms segregate as individuals or exhibit a strong clustering tendency, as observed in the post-processed APT data in Fig. 8 depends on several factors, with binding energy playing a particularly influential role. In this context, the binding energies between various solute pairs at dislocations within the ternary systems Mg–Al–Ca, Mg–Al–Zn and Mg–Zn–Ca was modeled using atomistic simulations. The analysis was restricted to solute pairs separated by first nearest neighbor distances. Notably, the calculated binding energies were found to be in strong agreement with those obtained from DFT calculations, as depicted in Fig. 9. While the data indicate that Ca clusters are energetically unfavorable in the bulk, corroborated by their sparse presence in Fig. 8, their abundance increases dramatically at the GB, being approximately 2- (Ca-pairs) and 12-fold (Ca-triplets) higher than those observed in the bulk, respectively. This substantial enrichment can be attributed to the favorable energetic landscape for clustering at the GB. More negative $\Delta E_{seg}^{I\text{-}J\prime\prime}$ values suggest that solute pairs are energetically favored at the GB over the bulk, whereas less positive values of $\Delta E_{bind}^{GB,I\text{-}J}$ indicate an increased propensity for solutes to remain clustered rather than dispersed at the GB.

4.2. Thermodynamic modeling of solute segregation at LAGB

With increasing overall solute concentration, it would be reasonable to anticipate that synergistic co-segregation effects and clustering tendencies become even more pronounced. Nevertheless, given the relatively low measured bulk concentrations (0.167 at.% for Al, 0.174 at.% for Ca and 0.333 at.% for Zn, the observed segregation behavior can largely be explained by a mono-segregation scenario as described by Eq. (2) and illustrated in Figs. 5d and e. Importantly, the spectra of ΔE_{seg} provide a qualitative reflection of the segregation levels measured via APT and effectively capture key features of solute distribution under these conditions.

For quantitative prediction of GB solute compositions beyond classical mono-segregation cases, three thermodynamic models were considered: McLean's model (no solute interactions), Fowler's model (incorporating identical-solute pair interactions), and Guttmann's model (accounting for all pairwise interactions including cross-species effects relevant beyond dilute limits) [83–85]. The Guttmann approach extends the Langmuir-McLean theory via an additional pair-interaction term ($\Delta E_{\mathrm{seg},i}^{\mathrm{pair}}$), expressed as:

$$\Delta E_{\mathrm{seg},i}^{\mathrm{pair}} = -2\left(\Omega_{\mathrm{GB}}^{\mathrm{I\text{-}M}} X_{\mathrm{GB}}^{\mathrm{I}} - \Omega_{\mathrm{b}}^{\mathrm{I\text{-}M}} X_{\mathrm{b}}^{\mathrm{I}}\right) + \sum_{I \neq J}\left(\Omega_{\mathrm{GB}}^{'\mathrm{I\text{-}J}} X_{\mathrm{GB}}^{\mathrm{J}} - \Omega_{\mathrm{b}}^{'\mathrm{I\text{-}J}} X_{\mathrm{b}}^{\mathrm{J}}\right), \tag{9}$$

which allows explicit treatment of co-segregation phenomena especially when local concentration exceeds dilute limits or when significant cluster formation occurs. The interaction parameter $\Omega^{\mathrm{I\text{-}J}}$ of solutes I and J at the sites i and j, respectively, depends on the coordination number Z of site i and the differences in bonding energies of solute pairs:

$$\Omega^{\mathrm{I\text{-}J}} = \frac{1}{2} Z \omega^{\mathrm{I\text{-}J}}, \tag{10}$$

where $\omega^{\mathrm{I\text{-}J}} = \Delta E^{\mathrm{I\text{-}J}} - \left(\Delta E^{\mathrm{I\text{-}I}} + \Delta E^{\mathrm{J\text{-}J}}\right)/2$.

The interaction coefficient $\Omega^{'\mathrm{I\text{-}J}}$ represents the net interaction between solutes I and J with respect to their interactions with the matrix element M:

$$\Omega^{'\mathrm{I\text{-}J}} = \Omega^{\mathrm{I\text{-}J}} - \Omega^{\mathrm{I\text{-}M}} - \Omega^{\mathrm{J\text{-}M}}. \tag{11}$$

The first term in Eq. (9) represents the Fowler interaction, which only considers I-I or J-J interactions. Recalling (2), the effective segregation energy becomes:

$$\Delta E_{\mathrm{seg},i}^{\mathrm{eff}} = \Delta E_{\mathrm{seg},i} + \Delta E_{\mathrm{seg},i}^{\mathrm{pair}} \tag{12}$$

The predictions from all three thermodynamic models using $\Delta E_{\mathrm{seg},i}$ and $\Delta E_{\mathrm{seg},i}^{\mathrm{eff}}$ were directly compared with experimentally determined solute concentrations obtained via APT within dislocation core regions defined by a radius of 6 nm across four distinct regions of interest outlined in Fig. 10a. The influence of pair interactions on predicted concentrations was found minimal, as illustrated in Fig. 10b. The slight differences among model predictions likely stem from the overall low system concentrations. The overall agreement between predicted and experimental values was reasonable, with the notable exception that Al concentration tends to be overestimated by all models.

4.3. Implications for grain boundary engineering

Overall, the findings in this paper emphasize that microstructural defects such as LAGBs serve as preferential sites for both mono-segregation and cooperative multi-solute segregation. These processes can significantly influence material behavior through defect chemistry modification. Specifically, the segregation of solute atoms like Ca, Al, and Zn at dislocations induces delocalization of core regions by expanding them over a broader area via local structural and chemical reordering. This reduces lattice distortions and weakens defect-defect interactions, which can fundamentally alter mechanical responses such as slip activation, ductility enhancement, GB mobility, and ultimately processing-structure–property relationships.

The observed tendency of Ca, Al and Zn to (co-)segregate along dislocation arrays at LAGB is consistent with our earlier study on AXZ310 magnesium alloy [28,29]. In that work, modification of a commercial AZ31 alloy with the addition of 0.3 wt.% Ca produced a thermally stable weak texture and a fine grain size, which together led to high strain hardening capability, enhanced ductility, and reduced plastic anisotropy. Building on that framework, the present atomistic analysis provides a mechanistic explanation for how Ca addition promotes texture weakening: synergistic solute segregation and clustering introduce a solute-drag effect that slows boundary migration during annealing, thereby impeding grain growth and stabilizing non-basal orientations.

A key outcome of this study is the explicit thermodynamic rationale underlying these effects. The calculated segregation and co-segregation energies reveal that Ca-containing pairs, while energetically unfavorable in the bulk, become markedly stabilized at LAGBs. This explains the strong solute enrichment seen in APT. This energetic picture complements our earlier findings on selective texture development controlled by solute-GB interactions, where solute segregation effectively pins GBs against coarsening and migration. Basu et al. [4] demonstrated that enhanced GB segregation (e.g. Gd > Dy) promotes selective growth of non-basal grains and improves room-temperature ductility, highlighting how solute drag can qualitatively modify texture evolution pathways. Similarly, Pei et al. [29] and Mouhib et al. [32] demonstrated that texture selection in Mg alloys depends strongly on the synergistic binding behavior of solute elements at GBs, for instance, co-adding Y to AZX310 amplifies Ca-driven GB co-segregation with Al and Zn.

Taken together with our previous work [28,29], the present results advocate for a GB engineering strategy for Mg alloys that leverages atomistically informed control of solute segregation. By strategically tuning solute selection and concentration ratios, it becomes possible to design GB chemistries that promote weak textures, fine and thermally stable microstructures, and superior mechanical properties, paving the way for next-generation, low-cost, and lightweight structural materials.

5. Conclusions

By coupling three-dimensional atom probe tomography with atomistic and thermodynamic modeling, the study delivers a chemically resolved and mechanism-based picture of how cooperative interactions between different substitutional solute species modulate both the magnitude and distribution of solute segregation at a representative low-angle grain boundary in a technologically relevant AZX010 magnesium alloy. The experimental results reveal an array of Ca-rich linear segregation zones that coincide with the tensile region of edge-dislocation cores, whereas Zn and Al preferentially occupy the complementary compressive regions. This highly ordered decoration on both sides of the core explains the periodic chemistry observed along the boundary plane.

Continuum elastic-dipole analysis revealed that large positive elastic dipoles make Ca atoms the primary ‘‘anchors’’ for tensile sites, while the smaller negative dipoles of Zn and Al stabilize the compressive sites. This misfit-controlled partitioning was confirmed by molecular-statics calculations, providing a multiscale rationalization of the experimental data. Furthermore, atomistic simulations show that Ca–Ca, Ca–Zn and Ca–Al pairs possess negative co-segregation energies, most pronounced within 8 Åof the dislocation core. This suggests that the low-angle boundary acts as a thermodynamic sink for Ca-rich pairs and larger clusters, mirroring the cluster statistics extracted from the APT data.

From an application standpoint, targeted Ca additions, balanced by a suitable amount of size-compensating solutes such as Zn or Al, could be used to control defect chemistry, and thus delocalize dislocation cores to enhance ductility, tune boundary mobility and texture

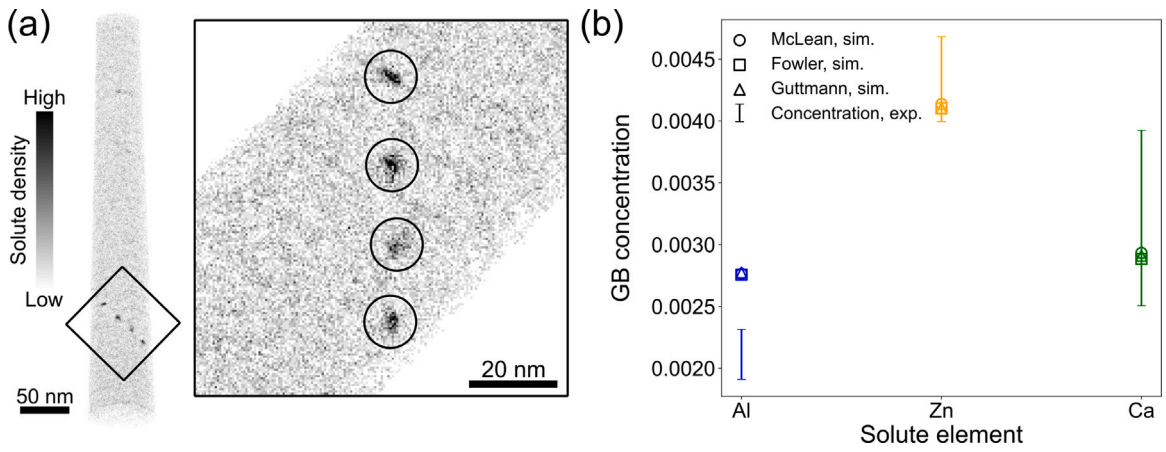

Fig. 10. Comparison of experimentally measured and theoretically predicted solute concentration at the LAGB. (a) In-plane solute distribution visualized along the dislocation array of the LAGB. (b) Solute concentration within 6 nm of the dislocation cores. Experimental bounds correspond to measurements from the four dislocation core regions marked in (a). Theoretical predictions of the GB solute concentrations are based on the McLean, Fowler, and Guttmann models, incorporating calculated segregation and solute-solute binding energies within 6 nm of the simulated dislocation core.

evolution through solute drag, and possibly stabilize fine recrystallized microstructures during thermo-mechanical processing.

Thermodynamic models incorporating calculated segregation energy spectra and pair interaction terms reproduce the experimentally measured Ca- and Zn-enrichment levels at the four probed dislocation cores of the boundary, but they systematically overshoot the Al level. The predictions for the three models, however, lie almost on top of one another, differing by only a few tenths of an at.%. The small spread implies that, for the present dilute bulk composition, the simple McLean isotherm (despite neglecting explicit solute–solute interactions) already captures the essential thermodynamics even when segregation elevates local GB concentrations by an order of magnitude. Further refinement of these models, including incorporation of entropy contributions, appears necessary before they can reliably predict and guide the optimization of interface chemistry in multi-component Mg alloys based on synergistic solute interactions.

CRediT authorship contribution statement

Risheng Pei: Conceptualization, Data curation, Formal analysis, Investigation, Visualization, Writing – original draft, Writing – review & editing. **Joé Petrazoller:** Investigation, Visualization, Writing – review & editing. **Achraf Atila:** Investigation, Writing – review & editing. **Simon Arnoldi:** Investigation. **Lei Xiao:** Investigation. **Xiaoqing Liu:** Investigation. **Hexin Wang:** Investigation, Writing – review & editing. **Sandra Korte-Kerzel:** Funding acquisition, Project administration, Supervision, Writing – review & editing. **Stéphane Berbenni:** Funding acquisition, Supervision, Writing – review & editing. **Thiebaud Richeton:** Funding acquisition, Writing – review & editing, Project administration, Supervision. **Julien Guénolé:** Funding acquisition, Supervision, Writing – review & editing. **Zhuocheng Xie:** Conceptualization, Data curation, Formal analysis, Funding acquisition, Investigation, Project administration, Supervision, Visualization, Writing – original draft, Writing – review & editing. **Talal Al-Samman:** Conceptualization, Funding acquisition, Project administration, Supervision, Writing – original draft, Writing – review & editing.

Declaration of competing interest

The authors declare that they have no known competing financial interests or personal relationships that could have appeared to influence the work reported in this paper.

Acknowledgments

R.P. and T.A.S. are grateful for the financial support from the German Research Foundation (DFG), Germany (Grant Nr. AL1343/7-1, AL1343/8-1 and Yi 103/3-1). H.W., Z.X. and T.A.S. acknowledge the financial support by the DFG (Grant Nr. 505716422). Z.X. and S.K.K. acknowledge financial support by the DFG, Germany through the projects A05 and C02 of the SFB1394 Structural and Chemical Atomic Complexity – From Defect Phase Diagrams to Material Properties, project ID 409476157. Additionally, Z.X. and S.K.K. are grateful for funding from the European Research Council (ERC) under the European Union's Horizon 2020 research and innovation programme (grant agreement No. 852096 FunBlocks). Z.X. acknowledges financial support funded by the DFG, Germany – Projektnummer 562592407 and 555365333. Fundings from the French National Research Agency (ANR), France grant ANR-21-CE08-0001 (ATOUUM) and grant ANR22-CE92-0058-01 (SILA) are acknowledged by J.G., T.R., and by S.B., J.G., J.P., T.R., respectively. The authors gratefully acknowledge the computing time provided to them at the NHR Center NHR4CES at RWTH Aachen University (project number p0020431). This is funded by the Federal Ministry of Education and Research, Germany, and the state governments participating on the basis of the resolutions of the GWK for national high performance computing at universities (www.nhr-verein.de/unsere-partner).

References

[1] D. Raabe, M. Herbig, S. Sandlöbes, Y. Li, D. Tytko, M. Kuzmina, D. Ponge, P.-P. Choi, Grain boundary segregation engineering in metallic alloys: A pathway to the design of interfaces, Curr. Opin. Solid State Mater. Sci. 18 (2014) 253–261.
[2] P. Lejček, S. Hofmann, Thermodynamics of grain boundary segregation and applications to anisotropy, compensation effect and prediction, Crit. Rev. Solid State Mater. Sci. 33 (2008) 133–163.
[3] S. Hofmann, P. Lejček, Solute segregation at grain boundaries, Interface Sci. 4 (1996) 241–267.
[4] I. Basu, K. Pradeep, C. Mießen, L. Barrales-Mora, T. Al-Samman, The role of atomic scale segregation in designing highly ductile magnesium alloys, Acta Mater. 116 (2016) 77–94.
[5] J. Weissmüller, Alloy effects in nanostructures, Nanostruct. Mater. 3 (1993) 261–272.
[6] K. Lücke, K. Detert, A quantitative theory of grain-boundary motion and recrystallization in metals in the presence of impurities, Acta Metall. 5 (1957) 628–637.
[7] J.W. Cahn, The impurity-drag effect in grain boundary motion, Acta Metall. 10 (1962) 789–798.
[8] Y. Huang, F. Humphreys, The effect of solutes on grain boundary mobility during recrystallization and grain growth in some single-phase aluminium alloys, Mater. Chem. Phys. 132 (2012) 166–174.

[9] J. Hirsch, T. Al-Samman, Superior light metals by texture engineering: Optimized aluminum and magnesium alloys for automotive applications, Acta Mater. 61 (2013) 818–843.
[10] J.P. Hadorn, K. Hantzsche, S. Yi, J. Bohlen, D. Letzig, J.A. Wollmershauser, S.R. Agnew, Role of solute in the texture modification during hot deformation of Mg-rare earth alloys, Met. Mater. Trans. A 43 (2012) 1347–1362.
[11] R. Pei, Z. Xie, S. Yi, S. Korte-Kerzel, J. Guénolé, T. Al-Samman, Atomistic insights into the inhomogeneous nature of solute segregation to grain boundaries in magnesium, Scr. Mater. 230 (2023) 115432.
[12] F. Mouhib, R. Pei, B. Erol, F. Sheng, S. Korte-Kerzel, T. Al-Samman, Synergistic effects of solutes on active deformation modes, grain boundary segregation and texture evolution in Mg-Gd-Zn alloys, Mater. Sci. Eng.: A 847 (2022) 143348.
[13] M.-N. Zhang, H.-L. Jia, M. Zha, L. Zhao, Z.-M. Hua, C. Wang, Y.-P. Gao, H.-Y. Wang, Anisotropic segregation-driven texture weakening in a dilute Mg-Al-Ca alloy during isothermal annealing, Mater. Res. Lett. 11 (2023) 781–788.
[14] D. Raabe, S. Sandlöbes, J. Millán, D. Ponge, H. Assadi, M. Herbig, P.-P. Choi, Segregation engineering enables nanoscale martensite to austenite phase transformation at grain boundaries: A pathway to ductile martensite, Acta Mater. 61 (16) (2013) 6132–6152.
[15] M. Hillert, Inhibition of grain growth by second-phase particles, Acta Metall. 36 (1988) 3177–3181.
[16] R. Pei, Y. Zou, D. Wei, T. Al-Samman, Grain boundary co-segregation in magnesium alloys with multiple substitutional elements, Acta Mater. 208 (2021) 116749.
[17] X. Zhao, H. Chen, N. Wilson, Q. Liu, J.-F. Nie, Direct observation and impact of co-segregated atoms in magnesium having multiple alloying elements, Nat. Commun. 10 (2019) 3243.
[18] Z. Zhang, J. Zhang, J. Xie, S. Liu, Y. He, R. Wang, D. Fang, W. Fu, Y. Jiao, R. Wu, Significantly enhanced grain boundary Zn and Ca co-segregation of dilute Mg alloy via trace Sm addition, Mater. Sci. Eng.: A 831 (2022) 142259.
[19] L. Li, Z. Li, A.K. da Silva, Z. Peng, H. Zhao, B. Gault, D. Raabe, Segregation-driven grain boundary spinodal decomposition as a pathway for phase nucleation in a high-entropy alloy, Acta Mater. 178 (2019) 1–9.
[20] L. Li, R.D. Kamachali, Z. Li, Z. Zhang, Grain boundary energy effect on grain boundary segregation in an equiatomic high-entropy alloy, Phys. Rev. Mater. 4 (2020) 053603.
[21] W. Xing, A.R. Kalidindi, D. Amram, C.A. Schuh, Solute interaction effects on grain boundary segregation in ternary alloys, Acta Mater. 161 (2018) 285–294.
[22] R. Wu, A.J. Freeman, G.B. Olson, First principles determination of the effects of phosphorus and boron on iron grain boundary cohesion, Science 265 (1994) 376–380.
[23] M. Seah, Interface adsorption, embrittlement and fracture in metallurgy: A review, Surf. Sci. 53 (1975) 168–212.
[24] S.J. Dillon, M. Tang, W.C. Carter, M.P. Harmer, Complexion: A new concept for kinetic engineering in materials science, Acta Mater. 55 (2007) 6208–6218.
[25] S. Korte-Kerzel, T. Hickel, L. Huber, D. Raabe, S. Sandlöbes-Haut, M. Todorova, J. Neugebauer, Defect phases–thermodynamics and impact on material properties, Int. Mater. Rev. 67 (1) (2022) 89–117.
[26] I.-H. Jung, M. Sanjari, J. Kim, S. Yue, Role of RE in the deformation and recrystallization of Mg alloy and a new alloy design concept for Mg–RE alloys, Scr. Mater. 102 (2015) 1–6.
[27] T. Trang, J. Zhang, J. Kim, A. Zargaran, J. Hwang, B.-C. Suh, N. Kim, Designing a magnesium alloy with high strength and high formability, Nat. Commun. 9 (2018) 2522.
[28] R. Pei, S. Korte-Kerzel, T. Al-Samman, Superior microstructure and mechanical properties of a next-generation AZX310 magnesium sheet alloy, Mater. Sci. Eng.: A 763 (2019) 138112.
[29] R. Pei, Y. Zou, M. Zubair, D. Wei, T. Al-Samman, Synergistic effect of y and Ca addition on the texture modification in AZ31B magnesium alloy, Acta Mater. 233 (2022) 117990.
[30] J. Nie, K. Oh-ishi, X. Gao, K. Hono, Solute segregation and precipitation in a creep-resistant Mg–Gd–Zn alloy, Acta Mater. 56 (2008) 6061–6076.
[31] H.-S. Jang, D. Seol, B.-J. Lee, A comparative study on grain boundary segregation and solute clustering in Mg-Al-Zn and Mg-Zn-Ca alloys, J. Alloys Compd. 894 (2022) 162539.
[32] F. Mouhib, Z. Xie, A. Atila, J. Guénolé, S. Korte-Kerzel, T. Al-Samman, Exploring solute behavior and texture selection in magnesium alloys at the atomistic level, Acta Mater. 266 (2024) 119677.
[33] P. Yi, T.T. Sasaki, S.E. Prameela, T.P. Weihs, M.L. Falk, The interplay between solute atoms and vacancy clusters in magnesium alloys, Acta Mater. 249 (2023) 118805.
[34] Z. Wang, M. Saito, K.P. McKenna, L. Gu, S. Tsukimoto, A.L. Shluger, Y. Ikuhara, Atom-resolved imaging of ordered defect superstructures at individual grain boundaries, Nature 479 (2011) 380–383.
[35] G.C. Sneddon, P.W. Trimby, J.M. Cairney, Transmission kikuchi diffraction in a scanning electron microscope: A review, Mater. Sci. Eng.: R: Rep. 110 (2016) 1–12.
[36] B. Gault, A. Chiaramonti, O. Cojocaru-Mirédin, P. Stender, R. Dubosq, C. Freysoldt, S.K. Makineni, T. Li, M. Moody, J.M. Cairney, Atom probe tomography, Nat. Rev. Methods Prim. 1 (2021) 51.
[37] C. Hu, R. Dingreville, B.L. Boyce, Computational modeling of grain boundary segregation: A review, Comput. Mater. Sci. 232 (2024) 112596.
[38] H. Wang, J. Guénolé, S. Korte-Kerzel, T. Al-Samman, Z. Xie, Defects in magnesium and its alloys by atomistic simulation: Assessment of semi-empirical potentials, Comput. Mater. Sci. 240 (2024) 113025.
[39] L. Huber, J. Rottler, M. Militzer, Atomistic simulations of the interaction of alloying elements with grain boundaries in Mg, Acta Mater. 80 (2014) 194–204.
[40] Z. Pei, R. Li, J.-F. Nie, J.R. Morris, First-principles study of the solute segregation in twin boundaries in Mg and possible descriptors for mechanical properties, Mater. Des. 165 (2019) 107574.
[41] M. Wagih, P.M. Larsen, C.A. Schuh, Learning grain boundary segregation energy spectra in polycrystals, Nat. Commun. 11 (2020) 6376.
[42] L. Karkina, I. Karkin, A. Kuznetsov, I. Razumov, P.A. Korzhavyi, Y.N. Gornostyrev, Solute–grain boundary interaction and segregation formation in Al: First principles calculations and molecular dynamics modeling, Comput. Mater. Sci. 112 (2016) 18–26.
[43] J. Zhang, Y. Dou, Y. Zheng, Twin-boundary segregation energies and solute-diffusion activation enthalpies in Mg-based binary systems: a first-principles study, Scr. Mater. 80 (2014) 17–20.
[44] L. Huber, B. Grabowski, M. Militzer, J. Neugebauer, J. Rottler, Ab initio modelling of solute segregation energies to a general grain boundary, Acta Mater. 132 (2017) 138–148.
[45] M. Wagih, C.A. Schuh, Grain boundary segregation beyond the dilute limit: Separating the two contributions of site spectrality and solute interactions, Acta Mater. 199 (2020) 63–72.
[46] Z. Zhang, C. Deng, Grain boundary segregation prediction with a dual-solute model, Phys. Rev. Mater. 8 (2024) 103605.
[47] Y. Cui, K. Song, Y. Bao, Y. Zhu, Q. Liu, P. Qian, Effect of cu and Mg co-segregation on the strength of the Al grain boundaries: A molecular dynamics simulation, Comput. Mater. Sci. 229 (2023) 112391.
[48] A. Ganguly, H. Wang, J. Guénolé, A. Prakash, S. Korte-Kerzel, T. Al-Samman, Z. Xie, Grain boundary segregation spectrum in basal-textured Mg alloys: From solute decoration to structural transition, Acta Mater. 283 (2024) 120556.
[49] V. Menon, S. Das, V. Gavini, L. Qi, Atomistic simulations and machine learning of solute grain boundary segregation in Mg alloys at finite temperatures, Acta Mater. 264 (2024) 119515.
[50] Z. Xie, A. Atila, J. Guénolé, S. Korte-Kerzel, T. Al-Samman, U. Kerzel, Predicting grain boundary segregation in magnesium alloys: An atomistically informed machine learning approach, J. Magnes. Alloy. (2025).
[51] C. He, Z. Li, H. Chen, N. Wilson, J.-F. Nie, Unusual solute segregation phenomenon in coherent twin boundaries, Nat. Commun. 12 (2021) 722.
[52] M. Wagih, C.A. Schuh, Can symmetric tilt grain boundaries represent polycrystals? Scr. Mater. 237 (2023) 115716.
[53] A. Stukowski, Visualization and analysis of atomistic simulation data with OVITO–the open visualization tool, Modelling Simul. Mater. Sci. Eng. 18 (1) (2009) 015012.
[54] P. Giannozzi, S. Baroni, N. Bonini, M. Calandra, R. Car, C. Cavazzoni, D. Ceresoli, G.L. Chiarotti, M. Cococcioni, I. Dabo, et al., QUANTUM ESPRESSO: a modular and open-source software project for quantum simulations of materials, J. Phys.: Condens. Matter. 21 (39) (2009) 395502.
[55] G. Kresse, D. Joubert, From ultrasoft pseudopotentials to the projector augmented-wave method, Phys. Rev. B 59 (3) (1999) 1758.
[56] P.E. Blöchl, Projector augmented-wave method, Phys. Rev. B 50 (24) (1994) 17953.
[57] J.P. Perdew, K. Burke, M. Ernzerhof, Generalized gradient approximation made simple, Phys. Rev. Lett. 77 (18) (1996) 3865.
[58] R. Fletcher, Practical Methods of Optimization, John Wiley & Sons, 2000.
[59] A.P. Thompson, H.M. Aktulga, R. Berger, D.S. Bolintineanu, W.M. Brown, P.S. Crozier, P.J. In't Veld, A. Kohlmeyer, S.G. Moore, T.D. Nguyen, et al., LAMMPS-a flexible simulation tool for particle-based materials modeling at the atomic, meso, and continuum scales, Comput. Phys. Comm. 271 (2022) 108171.
[60] H.-S. Jang, D. Seol, B.-J. Lee, Modified embedded-atom method interatomic potential for the Mg–Zn–Ca ternary system, Calphad 67 (2019) 101674.
[61] H.-S. Jang, D. Seol, B.-J. Lee, Modified embedded-atom method interatomic potentials for Mg–Al–Ca and Mg–Al–Zn ternary systems, J. Magnes. Alloy. 9 (1) (2021) 317–335.
[62] J.D. Honeycutt, H.C. Andersen, Molecular dynamics study of melting and freezing of small lennard-jones clusters, J. Phys. Chem. 91 (19) (1987) 4950–4963.
[63] P. Hirel, Atomsk: A tool for manipulating and converting atomic data files, Comput. Phys. Comm. 197 (2015) 212–219.
[64] E. Bitzek, P. Koskinen, F. Gähler, M. Moseler, P. Gumbsch, Structural relaxation made simple, Phys. Rev. Lett. 97 (17) (2006) 170201.
[65] J. Guénolé, W.G. Nöhring, A. Vaid, F. Houllé, Z. Xie, A. Prakash, E. Bitzek, Assessment and optimization of the fast inertial relaxation engine (fire) for energy minimization in atomistic simulations and its implementation in lammps, Comput. Mater. Sci. 175 (2020) 109584.
[66] D. McLean, A. Maradudin, Grain Boundaries in Metals, American Institute of Physics, 1958.
[67] C. White, W. Coghlan, Spectrum of binding energies approach to grain boundary segregation, Met. Trans. A;(United States) 8 (9) (1977).

[68] W. Read, W. Shockley, Dislocation models of crystal grain boundaries, Phys. Rev. 78 (1950) 275–289.
[69] F. Frank, The resultant content of dislocations in an arbitrary intercrystalline boundary, in: Symposium on the Plastic Deformation of Crystalline Solids, Mellon Institute, Pittsburgh,(NAVEXOS-P-834), vol. 150, 1950.
[70] B. Bilby, Bristol conference report on defects in crystalline materials, vol. 123, Phys. Soc., London, 1955.
[71] A. Love, A Treatise on the Mathematical Theory of Elasticity, the University Press, 1959.
[72] E. Kröner, Allgemeine Kontinuumstheorie der Versetzungen und Eigenspannungen, Arch. Ration. Mech. Anal. 4 (1) (1959) 273–334.
[73] R. Siems, Mechanical Interactions of Point Defects, Phys. Status Solidi (B) 30 (2) (1968) 645–658.
[74] G. Leibfried, N. Breuer, Point Defects in Metals I: Introduction to the Theory, Springer, 1978.
[75] R.W. Balluffi, Introduction to Elasticity Theory for Crystal Defects, second ed., World Scientific, 2016.
[76] E. Clouet, C. Varvenne, T. Jourdan, Elastic modeling of point-defects and their interaction, Comput. Mater. Sci. 147 (2018) 49–63.
[77] G. Gengor, O. Celebi, A. Mohammed, H. Sehitoglu, Continuum strain of point defects, J. Mech. Phys. Solids 188 (2024) 105653.
[78] J. Petrazoller, J. Guénolé, S. Berbenni, T. Richeton, On the effect of elastic anisotropy and polarizability on solute segregation at low-angle grain boundaries, Comput. Mater. Sci. 249 (2025) 113642.
[79] D.N. Demidov, A.B. Sivak, P.A. Sivak, New method for calculation of radiation defect dipole tensor and its application to di-interstitials in copper, Symmetry 13 (7) (2021) 1154.
[80] A. Torres-Sánchez, J.M. Vanegas, M. Arroyo, Examining the Mechanical Equilibrium of Microscopic Stresses in Molecular Simulations, Phys. Rev. Lett. 114 (25) (2015) 258102.
[81] C. Elsässer, T. Elsässer, Codoping and grain-boundary cosegregation of substitutional cations in α-Al2O3: A density-functional-theory study, J. Am. Ceram. Soc. 88 (1) (2005) 1–14.
[82] D. Scheiber, L. Romaner, R. Pippan, P. Puschnig, Impact of solute-solute interactions on grain boundary segregation and cohesion in molybdenum, Phys. Rev. Mater. 2 (9) (2018) 093609.
[83] R.H. Fowler, Statistical Thermodynamics, CUP Archive, 1939.
[84] M. Guttmann, Equilibrium segregation in a ternary solution: A model for temper embrittlement, Surf. Sci. 53 (1) (1975) 213–227.
[85] M. Guttmann, D. McLean, Grain boundary segregation in multicomponent systems, Interfacial Segreg. (1979) 261–348.